J. Fluid Mech. (2006), *vol.* 569, *pp.* 89–111. © 2006 Cambridge University Press
doi:10.1017/S0022112006002503 Printed in the United Kingdom

The fall of a viscous thread onto a moving surface: a 'fluid-mechanical sewing machine'

By S. CHIU-WEBSTER AND J. R. LISTER

Institute of Theoretical Geophysics, Department of Applied Mathematics and Theoretical Physics, University of Cambridge, Wilberforce Road, Cambridge CB3 0WA, UK

(Received 21 October 2005 and in revised form 26 May 2006)

A viscous thread falling onto a steadily moving horizontal belt shows a surprisingly complex range of behaviour in experiments. Low belt speeds produce coiling, as might be expected from the behaviour of a thread falling onto a stationary surface. High belt speeds produce a steady thread, whose shape is predicted well by theory developed to describe a stretching viscous catenary with surface tension and inertia. Intermediate belt speeds show several novel modes of oscillation, which lay down a wide variety of patterns on the belt. The patterns include meanders, side kicks, slanted loops, braiding, figures-of-eight, Ws, and also period-doubled versions of figures-of-eight, meanders and coiling. The experimental boundary between steady and unsteady behaviour occurs at a slightly lower belt speed than the loss of the steady solution for a stretching catenary.

1. Introduction

The buckling instability that results from competition between axial compression and lateral bending is a well-known phenomenon in the mechanical behaviour of solid beams and shells. Viscous threads and sheets also undergo a buckling instability, as may be simply demonstrated with honey or syrup poured onto toast from a sufficient height. A thread of honey undergoes a helical motion about the vertical, sometimes referred to as the 'fluid rope-coil' effect, and a sheet of honey folds back and forth periodically.

Coiling of a viscous thread has been extensively studied (e.g. Barnes & Woodcock 1958; Barnes & MacKenzie 1959; Cruickshank & Munson 1983; Griffiths & Turner 1988). Taylor (1969) perceived that axial compression was necessary for the buckling to occur. Mahadevan, Ryu & Samuel (1998, 2000) identified an inertia-dominated case in which centripetal torques balance bending stresses in the coil and showed that the consequent scaling law for the coiling frequency agreed with experiments. Ribe (2004) used a numerical approach to calculate steady coiling solutions over a large frequency range, and identified three distinct modes of coiling – viscous, gravitational and inertial – with three different scaling laws. Ribe's results were verified experimentally by Maleki *et al.* (2004). A fourth scaling law is described in Ribe *et al.* (2006).

The periodic folding of a viscous sheet has also been studied (Skorobogatiy & Mahadevan 2000; Ribe 2003). A comparison between coiling and the folding problem, as well as between viscous coiling and the coiling of an elastic rope (Mahadevan & Keller 1996), may be found in Ribe (2004).

We consider the novel problem of a viscous fluid thread falling onto a horizontally translating surface (figure 1). Fluid of kinematic viscosity ν is released at volumetric

https://doi.org/10.1017/S0022112006002503 Published online by Cambridge University Press

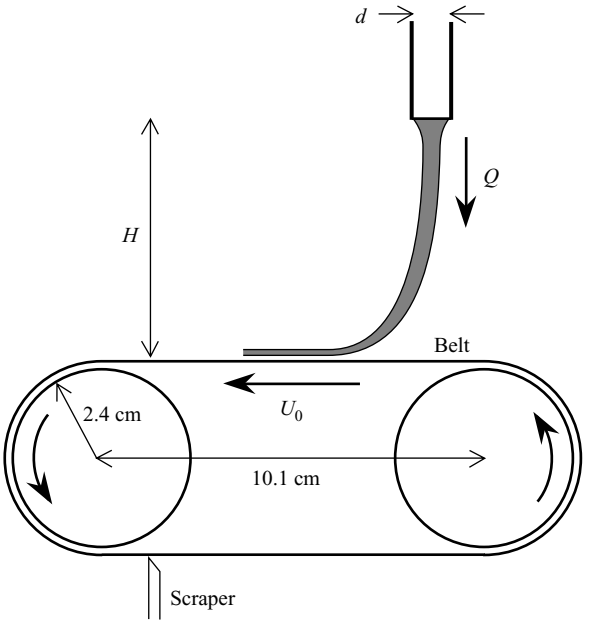


FIGURE 1. Geometry of the problem. A fluid thread falls a distance H with volume flux Q from a nozzle of internal diameter d onto a horizontal surface moving with velocity U_0. The experimental implementation uses a rubber belt wrapped around two rotating cylinders as shown.

flow rate Q from a nozzle of diameter d, and falls a height H onto a horizontal belt moving at speed U_0. The motion of the belt breaks the rotational symmetry, and thereby allows the thread to exhibit new and wide-ranging behaviour that includes steady solutions, apparently chaotic behaviour, and a striking number of modes of periodic oscillation. For much of the parameter range there are noticeable hysteretic effects and it is also possible to see period-doubled modes of oscillation. Both the fundamental and the period-doubled oscillations lay down regular patterns on the moving surface, which, pursuing the imagery of 'fluid rope-coiling', might be described as the stitching patterns of a 'fluid-mechanical sewing machine'.

The paper is organized as follows. In § 2, we describe the experimental method. In § 3, we present the experimental results, together with a regime diagram and photographs of the regular patterns on the belt that can be produced by the periodic oscillations of the thread. The regime diagram and photographs summarize the main features of the patterns and their occurrence in parameter space, and further details of the observed phenomena are described in the text.

In § 4, we derive a simple theory for a steady stretching fluid catenary, which neglects resistance to bending, but includes viscous, gravitational, capillary and inertial forces. The governing equations and numerical method of solution are summarized. In § 5, we compare and find excellent agreement between predicted shapes obtained from numerical integration and digital images from the experiments, as well as horizontal displacement of the thread. Careful measurements are also presented for the first stability boundary, at which the thread undergoes a bifurcation from a steady viscous catenary either to a sideways sinusoidal oscillation or to a more episodic motion, which we term 'side kicks' and describe further below. The loss of the theoretical solution when the tension at the bottom of the catenary becomes zero compares

https://doi.org/10.1017/S0022112006002503 Published online by Cambridge University Press

Experiment	Added water (wt%)	ρQ (g min^{-1})	d (cm)	θ start (°C)	θ end (°C)	ν start (cm^2 s^{-1})	ν end (cm^2 s^{-1})
1	0	2.13	1.00	21.00	21.00	375	375
2	0	1.65	0.65	20.75	21.00	390	375
3	0	2.03	0.80	20.75	20.50	390	406
4	0	2.30	0.80	21.75	21.75	334	334
5	0	3.80	1.00	21.50	21.50	347	347
6	1.25	3.33	0.65	22.00	22.50	225	208
7	2.50	4.93	0.65	21.25	20.25	113	117
8	2.50	5.90	0.80	21.25	22.00	117	105
9	0	1.68	0.80	21.75	21.25	334	361

TABLE 1. Experimental parameters: ρQ is the mass flux, d the internal diameter of the steel tube, θ the temperature, and ν the kinematic viscosity calculated from (A 1).

reasonably well with the experimentally determined stability boundary. In § 6, we discuss the results and avenues for future investigation.

2. Experimental method

Tate & Lyle's Golden Syrup, either pure or diluted with 1.25 or 2.50 wt% added water, was fed from a constant-head reservoir through a steel tube of known internal diameter d, and allowed to fall onto the horizontal upper surface of a moving rubber belt (figure 1). The belt was wrapped around two horizontal Perspex cylinders to form a loop and the cylinders were rotated using a variable-speed motor. To remove fluid from the belt before it returned to the horizontal section at the top of the loop, a rubber scraper was placed at the bottom section of the loop. The dimensions of the apparatus are shown in figure 1.

Experiments were conducted with a given flow rate Q, tube diameter and working fluid (table 1). In each experiment, the belt speed U_0 could be varied continuously using the motor setting over the approximate range 1–20 cm s^{-1}. The fall height H was varied in discrete 0.5 cm steps over the range 4.5–19 cm using an adjustable platform. The methods for calculating the viscosity ν, density ρ and surface tension γ are described in Appendix A.

The mass flux ρQ was measured to 1 % accuracy by weighing the fluid collected by a container over 2 min, before and after each experiment. The belt speeds along the boundary between steady and oscillatory flow were generally measured at the relevant setting of the motor by timing a fixed number of revolutions with a 50 frames s^{-1} video camera. For the more extensive exploration of boundaries between different oscillatory regimes, the belt speed was first calibrated against the motor setting to obtain a quadratic fit, from which the belt speed could be inferred for other settings. In both cases, there appeared to be small variations in belt speed during one revolution of up to ± 5 %, perhaps because of variation in the tension in different parts of the rubber belt caused by the scraper underneath. These variations did not, however, significantly affect the results reported below.

3. Experimental results

3.1. *Overview*

The primary distinction in the type of behaviour observed is between steady flow, which is found for sufficiently large belt speeds, and a variety of oscillatory or unsteady

https://doi.org/10.1017/S0022112006002503 Published online by Cambridge University Press

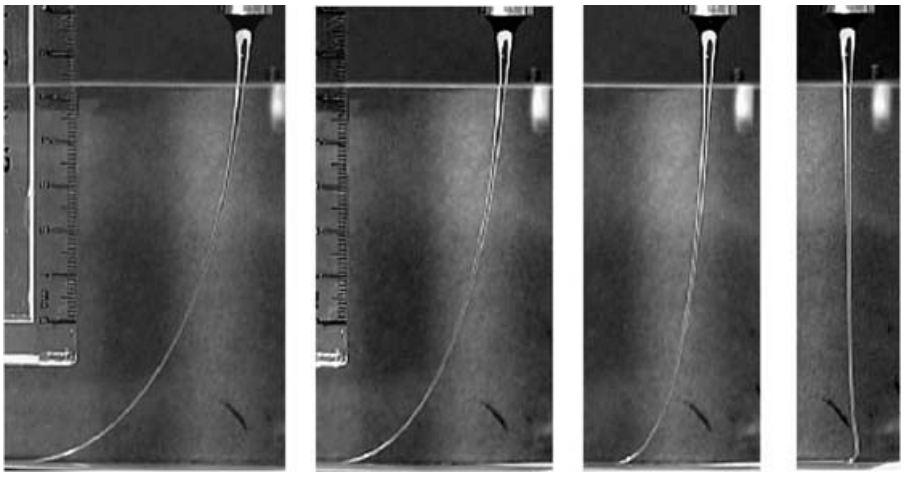


FIGURE 2. Steady shapes in a representative experiment (experiment 1) with $h = 10\,\mathrm{cm}$ and $U_0 = 17.7$, 14.1, 10.5, $7.5\,\mathrm{cm\,s^{-1}}$, respectively. The belt is moving from right to left in all cases. The deflection of the thread to the right, forming a 'heel', for $U_0 = 7.5\,\mathrm{cm\,s^{-1}}$ is indicative of buckling under compression, but the shape is nevertheless steady.

flows, which are found for smaller belt speeds. The boundary between steady and oscillatory behaviour is well-defined and described further in § 5.2.

Figure 2 shows a representative progression of thread shapes in the steady regime as the belt speed U_0 is decreased at fixed fall height H towards the boundary with oscillatory behaviour. The thread forms a steady catenary. For the larger values of U_0, the thread is being stretched throughout its length in the direction of the belt motion, as evidenced by the thinning of the thread. Comparison with theory is given in § 5. As U_0 is decreased, the thread becomes more vertical and the total horizontal displacement from the nozzle to the contact with the belt decreases. At the lowest speed in figure 2 ($U_0 = 7.5\,\mathrm{cm\,s^{-1}}$), the thread bends backwards in the opposite direction to U_0 and has a 'heel' shape near the belt suggestive of compressional stresses and buckling. The shape is nevertheless steady and remains in the vertical plane defined by the belt motion and the nozzle. Such a heel shape is typical for steady flows at belt speeds just above the boundary with unsteady behaviour.

As U_0 is reduced just below this boundary, the thread begins to oscillate out of the plane of belt motion in one of two regimes, which we term 'meanders' and 'side kicks' and describe further in § 3.2. Typical patterns produced on the belt in these regimes are shown in figure 3(b, c). For sufficiently small values of U_0, the thread undergoes a coiling motion, as might be expected from the behaviour of a viscous thread falling onto a stationary surface. Combined with the translation of the belt, the coiling motion produces a pattern on the belt of the form shown in figure 3(d).

For values of the belt speed intermediate between the slightly subcritical values that definitely give meanders or side kicks and the near-zero values that definitely give coiling, a variety of more complicated modes of oscillation are possible. We first catalogue the possibilities in § 3.2 in order to develop some descriptive terminology. In § 3.3, we then describe where the different modes occur in the parameter space (H, U_0) of a typical experiment and the sequence of transitions as U_0 is varied for different values of H. The boundary with steady behaviour and the steady shapes are further discussed in § 5, following development of the theory in § 4.

https://doi.org/10.1017/S0022112006002503 Published online by Cambridge University Press

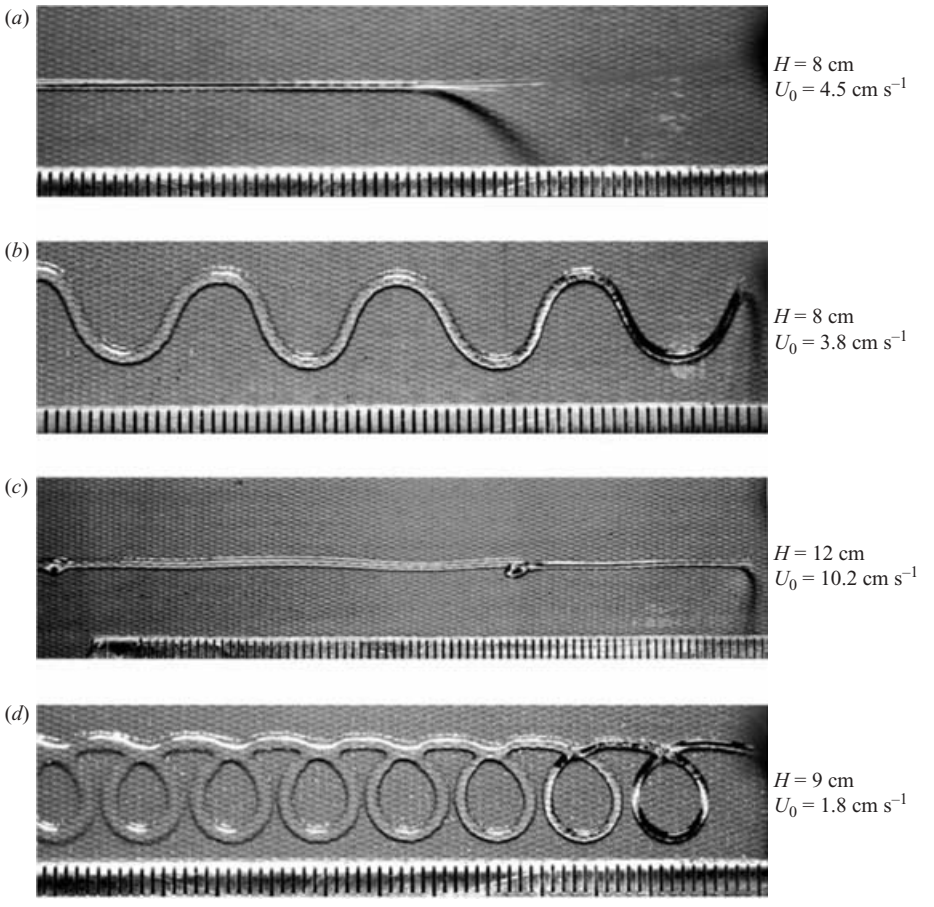


FIGURE 3. View from above of the following patterns: (*a*) steady, (*b*) sinusoidal meanders, (*c*) side kicks and (*d*) coiling. The scale is in millimetres and the motion is from right to left. $\rho Q = 1.80\,\mathrm{g\,min^{-1}}$, $d = 8.0\,\mathrm{mm}$, $\nu \leqslant 390\,\mathrm{cm^2\,s^{-1}}$. The value of ν is approximate here since the strong lighting used to take these photographs would have heated the syrup.

3.2. *Patterns and modes of oscillation*

We categorize the modes of oscillation by the patterns that the thread lays down on the belt. 'Meanders', 'side kicks' and 'coiling' have already been mentioned and are shown in figure 3.

Meanders near the steady–unsteady boundary have small amplitudes and appear to be almost a pure sine wave. As U_0 is reduced, the apparently sinusoidal form persists to amplitudes comparable with the wavelength (figure 3*b*) and the motion of the overlying thread remains predominantly a simple oscillation in the direction perpendicular to the belt motion.

Further increase in the amplitude-to-wavelength ratio, largely associated with a decrease in wavelength, produces 'bunched-up' meanders (figure 4*a*) which deviate markedly from sinusoidal form; the overlying thread executes a figure-of-eight oriented perpendicular to the direction of belt motion and with the thread motion at the extremes of the '8' oriented *against* the direction of belt motion. A closely related pattern is 'braiding' (figure 4*b*) in which the direction of motion is qualitatively the same as that of bunched-up meanders, but successive loops of the pattern laid

https://doi.org/10.1017/S0022112006002503 Published online by Cambridge University Press

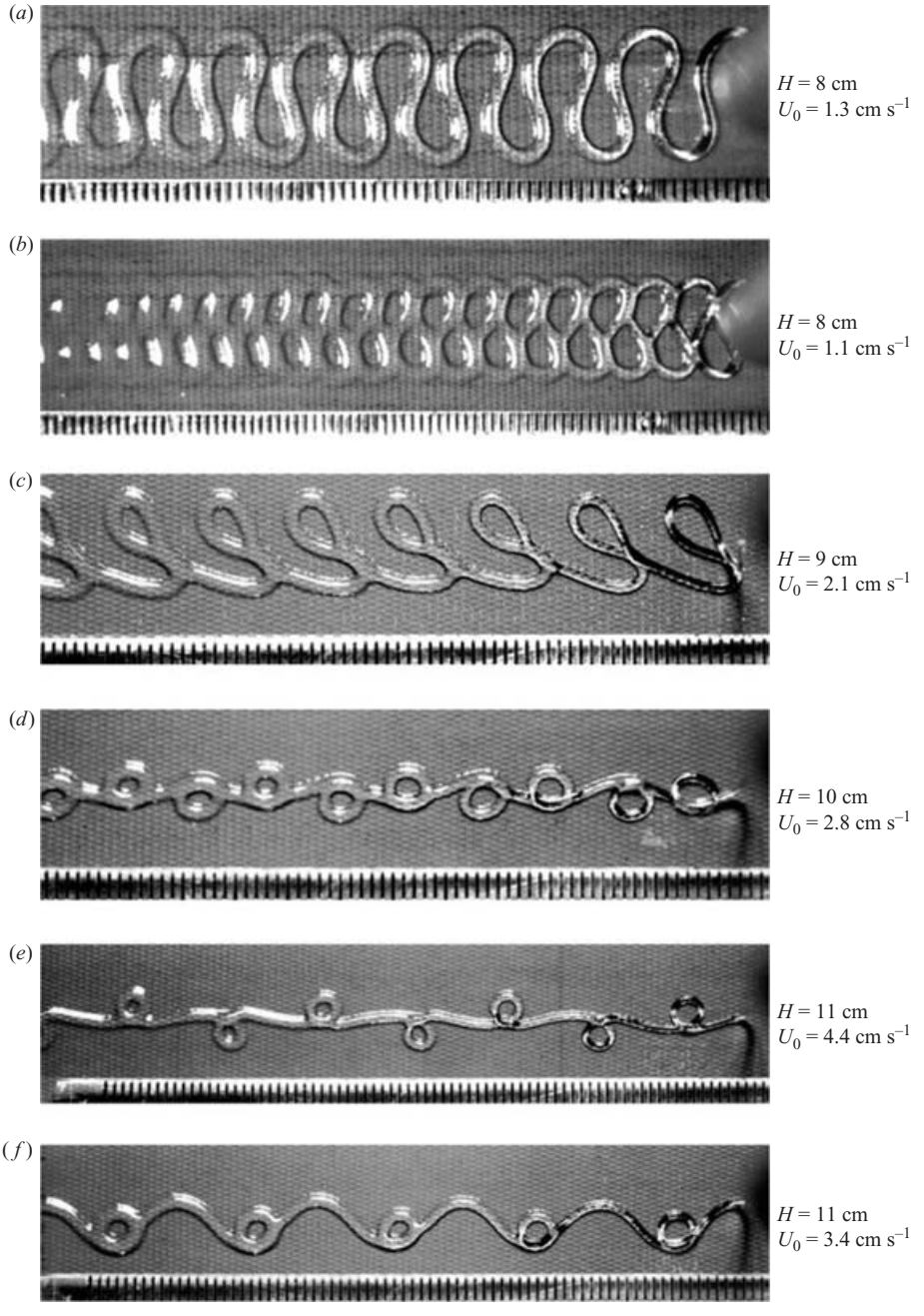


FIGURE 4. Photographs of patterns: (*a*) bunched-up meanders, (*b*) braiding, (*c*) slanted loops, (*d*, *e*) figures-of-eight, (*f*) the W pattern. For (*a*, *b*) $\rho Q = 3.05\,\mathrm{g\,min^{-1}}$, $d = 8.0\,\mathrm{mm}$, $\nu \leqslant 330\,\mathrm{cm^2\,s^{-1}}$, and for (*c*–*f*) $\rho Q = 1.80\,\mathrm{g\,min^{-1}}$, $d = 8.0\,\mathrm{mm}$, $\nu \leqslant 390\,\mathrm{cm^2\,s^{-1}}$. The value of ν is again approximate owing to the strong lighting.

down are fused on both sides. The pattern 'slanted loops' (figure 4*c*) also involves a figure-of-eight motion of the thread, but the orientation of the '8' is not in this case perpendicular to the belt motion and varies with the belt speed. The direction

https://doi.org/10.1017/S0022112006002503 Published online by Cambridge University Press

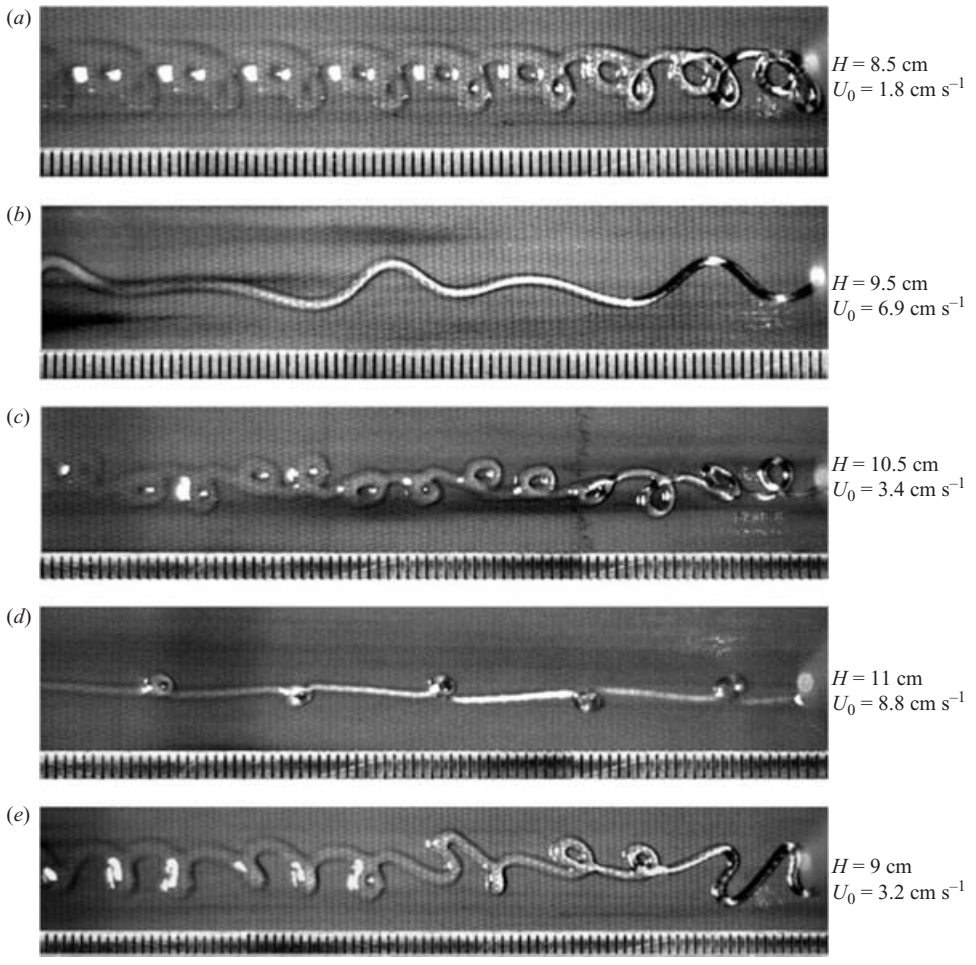


FIGURE 5. Photographs of patterns characteristic of larger heights: the period-doubled oscillations (*a*) 'double coils', (*b*) 'double meanders', (*c*) 'double-8's; (*d*) the tight figure-of-eight produced by alternating side kicks and (*e*) irregular behaviour. $\rho Q = 3.05\,\mathrm{g\,min^{-1}}$, $d = 8.0\,\mathrm{mm}$, $\nu \leqslant 330\,\mathrm{cm^2\,s^{-1}}$. The value of ν is again approximate owing to the strong lighting.

in which the pattern is traced is the same as that of large-amplitude meanders and braiding, but the pattern is fused on one side.

A 'figure-of-eight' pattern can also be laid down on the belt itself (figure 4*d*, *e*). The corresponding motion of the thread is again a figure-of-eight, but now with the thread motion at the extremes of the '8' oriented in the *same* direction as the belt motion; the loops of the figure-of-eight pattern on the belt are thus traced in the opposite direction to those of braiding and slanted loops. A somewhat surprising breaking of symmetry about the centreline is provided by W patterns (figure 4*f*), which might be thought of as either a 'figure-of-eight' pattern with the loops on one side missing, or meandering with loops added on one side of the meander and not the other.

All the above patterns have regions of stability in parameter space in which, once formed, the pattern is repeatable, regular and observable indefinitely. Variations of some of the patterns can be formed by period-doubling bifurcations. Figure 5(*a*) shows an example of 'double-coiling' (cf. figure 3*d*) in which successive coils alternate in size and fuse in pairs. The 'double-meander' (figure 5*b*) is a meandering pattern with

https://doi.org/10.1017/S0022112006002503 Published online by Cambridge University Press

alternate large and small oscillations. Both double-coiling and double-meandering can be observed indefinitely for some parameter values, but can also evolve over 5–20 oscillations to simple coiling and meandering, respectively, for other values. Double-coiling is more likely to be stable.

The 'double-8' pattern (figure 5*c*) is so-called because it is laid-down in a similar fashion to the 'figure-of-eight' (figure 4*d*, *e*) but with two loops on alternate sides instead of one loop. It is much less stable and harder to find.

Finally, we return to 'side kicks' (figure 3*c*), which are episodic disturbances to an almost steady near-vertical thread with a noticeable heel. In a single 'kick', the heel buckles and collapses suddenly to one side, the thread is dragged forward with the belt and then slowly falls back to reform the heel. The pattern on the belt is almost straight with a kink formed by the sudden collapse of the heel. The kicks occur with a well-defined period, but the side on which the kick occurs usually seems to follow a random sequence. It is, however, possible for kicks to occur on alternate sides and to form a figure-of-eight pattern with very small loops (figure 5*d*).

Whereas the coiling and sinusoidal meander patterns are largely the products, respectively, of simple helical and transverse oscillations of the thread with the linear belt motion, the other patterns require more complicated motion of the thread. Visual impressions of the motion of different parts of the thread during oscillations and the narrow parameter regime in which some of the patterns occur (see § 3.3) suggest that different modes of deformation of the parts of the thread need to interact with related time scales. We also note that when the base of the thread touches a previous part of the pattern, it appears to have a significant effect on the oscillation, as evidenced most clearly in the tilt of 'slanted loops' and the fusing of pairs of loops in 'double-coiling'.

3.3. *Regime diagram*

Having catalogued the variety of possible patterns, we now attempt to describe when they occur in a typical experiment as U_0 is varied at given values of the fall height H. There are two reasons why it is not possible to give a complete description that includes the stability boundaries of all the different patterns. First, some of the regions of stability in parameter space are small and, with the $\pm 5\,\%$ variation in belt speed during a revolution and the 0.5 cm discrete steps used to vary H, it was not possible to identify the stability boundary with sufficient precision relative to the size of the region. Secondly, in much of the parameter space there are significant hysteresis loops, so that a number of patterns can be stable for given values of U_0 and H, and which one is observed depends on the history of variation.

Three major stability boundaries could be determined with sufficient precision and repeatability to be plotted on a regime diagram. These are the boundary between steady flow and unsteady flow (meanders or side kicks), the loss of stability of meanders as U_0 is decreased, and the loss of stability of coiling as U_0 is increased. The boundary between steady and unsteady flow is not noticeably hysteretic for small heights (e.g. $H \lesssim 9$ cm in experiment 3) and only slightly hysteretic (about 5 %) at larger heights; hence the appearance of unsteadiness as U_0 is decreased and the disappearance of unsteadiness as U_0 is increased will be considered to occur at the same value of U_0. The other two boundaries are not noticeably hysteretic for sufficiently small heights, but are strongly hysteretic at larger heights.

The regime diagram for a typical experiment (experiment 3) is shown in figure 6, in which, motivated by the theoretical considerations of § 4, we have used $U_0^{1/2}$ as a parameter rather than U_0. The three boundaries described above are plotted as lines constrained by the data points shown. It can be seen that for $8.5\,\text{cm} \lesssim H \lesssim 11\,\text{cm}$ there

https://doi.org/10.1017/S0022112006002503 Published online by Cambridge University Press

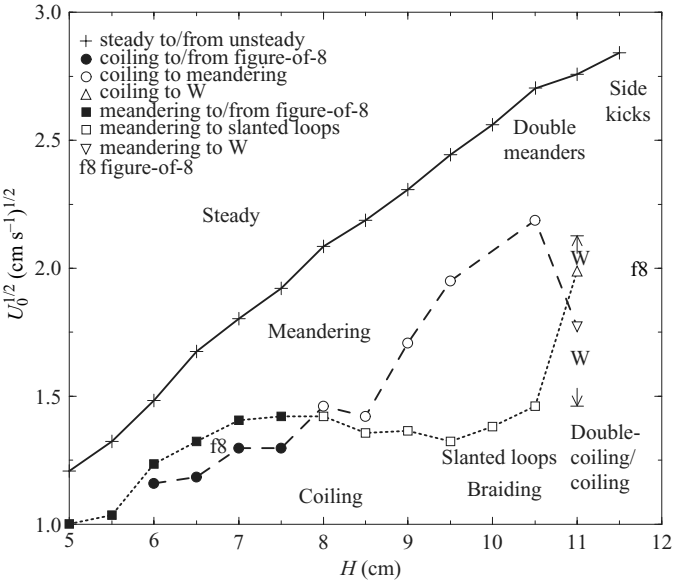


FIGURE 6. Regime diagram for experiment 3. The three lines represent the boundary between steady and unsteady behaviour (solid), the loss of stability of coiling as U_0 increases (dashed) and the loss of stability of meandering as U_0 decreases (dotted). The symbols denote the pattern change as the stability boundary is crossed (see key), with open symbols used for hysteretic (irreversible) changes. The W-pattern is found at $H = 11$ cm over the range of U_0 indicated by the arrows. The locations of the braiding, slanted loops, double-meandering and double-coiling and large-H figure-of-eight regimes are approximate, because their stability boundaries could not be determined with precision.

is a large hysteresis loop in which both coiling and meandering are stable. Conversely, for $5\,\text{cm} \lesssim H \lesssim 8\,\text{cm}$ there is a region in which neither coiling nor meandering is stable and where something else, in fact figures-of-eight, must occur.

The approximate locations of other patterns (slanted loops, braiding, the W-pattern, side kicks, the period-doubled patterns and a second region of figures-of-eight) are also shown, though it was not possible to determine their stability boundaries. Owing to hysteresis, some of these patterns are obtained as U_0 is varied in a particular direction: for example, slanted loops are obtained from meandering by decreasing U_0. Further discussion of the regime diagram is best organized by considering the following height ranges in turn: $H \lesssim 7.5\,\text{cm}$, $8\,\text{cm} \lesssim H \lesssim 10.5\,\text{cm}$, $H \approx 11\,\text{cm}$ and $H \gtrsim 11.5\,\text{cm}$.

$H \lesssim 7.5\,cm$

Hysteretic effects are not noticeable and there is either a reversible sequence of transitions between meanders, figures-of-eight and coiling or a direct reversible transition between meanders and coiling. (Extension of the transition curves to smaller heights was not possible because of the minimum belt speed of $1\,\text{cm}\,\text{s}^{-1}$.)

$8\,cm \lesssim H \lesssim 10.5\,cm$

The stability boundaries of coiling and meandering cross at about $H = 8$ cm. Over the range $8.5\,\text{cm} \lesssim H \lesssim 10.5\,\text{cm}$, there is significant hysteresis with both meandering and coiling obtainable in the region between the circles and the squares. As U_0 is increased slowly from a small value, coiling first becomes unstable (circles) to meandering, and meandering then disappears (plus signs) to give a steady catenary.

https://doi.org/10.1017/S0022112006002503 Published online by Cambridge University Press

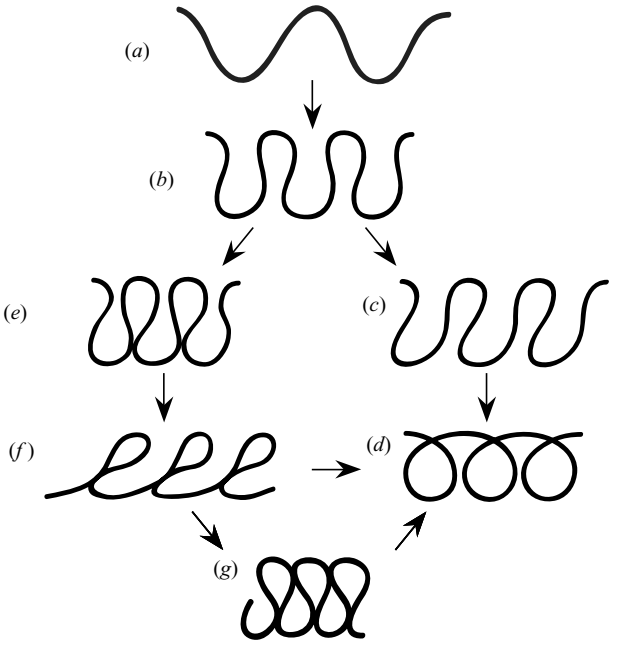


FIGURE 7. Possible stages between meandering and translated coiling, as U_0 is decreased in the range $8\,\text{cm} \leqslant H \leqslant 10.5\,\text{cm}$. The transition (e)–(f) occurs with time at fixed U_0. The transitions to (d) occur via an instability.

As U_0 is decreased slowly, the steady catenary becomes unstable (plus signs) to sinusoidal meanders (figure 7*a*), but meandering then persists to much smaller values of U_0. As the stability boundary (squares) is approached, the meanders become increasingly bunched-up (figure 7*b*) owing to the decrease in belt speed, while the amplitude and frequency of oscillation remain roughly constant. The subsequent sequence of transitions depends on H.

For $H \approx 8\,\text{cm}$ and $8.5\,\text{cm}$, the bunched-up meanders start to slant to one side (figure 7*c*), become unstable and then undergo a transition to coiling (figure 7*d*). For $9 \lesssim H \lesssim 10.5\,\text{cm}$, the bunched-up meanders persist on decrease of U_0 until the bunching causes two consecutive loops to just touch (figure 7*e*), which typically occurs on one side first owing to small experimental asymmetries. As soon as touching occurs (i.e. without further decrease of U_0), the orientation of the thread's figure-of-eight motion starts to rotate, the overlap on the touching side increases with successive oscillations and a slanted-loop pattern (figure 7*f*) begins to form.

For $H \approx 9\,\text{cm}$, the slanted-loop pattern does not reach an equilibrium orientation, but becomes unstable after some 3–10 oscillations to yield translated coiling. For $H \gtrsim 9.5\,\text{cm}$, the slanted loops reach an equilibrium stable orientation. On further decrease of U_0, slanted loops become unstable to translated coiling (figure 7*d*) for $H \approx 9.5\,\text{cm}$ and $H \approx 10.5\,\text{cm}$, and to braiding for $H \approx 10\,\text{cm}$ (figure 7*d*, *g*). Braiding is stable and persists on further decrease in U_0 almost to zero, where the loops start to overlap; it even persists for a few oscillations when U_0 is reduced to zero, before finally undergoing a transition to coiling.

$H \approx 11\,cm$

For $H \approx 11\,\text{cm}$, there are a number of possibilities: the W-pattern, meandering and coiling, and the period-doubled patterns double-meandering and double-coiling.

https://doi.org/10.1017/S0022112006002503 Published online by Cambridge University Press

The W-pattern is stable and occurs for belt speeds intermediate between those that give forms of meandering and coiling. The transitions between W and coiling and between W and meandering are hysteretic and hard to pin down. As noted earlier, double-meandering and double-coiling can be observed indefinitely, or can evolve to simple meandering and coiling, respectively.

$11.5\,cm \lesssim H \lesssim 18.5\,cm$

For $H \gtrsim 11.5$ cm, the regime diagram is even harder to define because the lower part of the thread, being thin and highly stretched, is sensitive to small perturbations. Regular modes of oscillation become unstable as H increases and give way to irregular modes of oscillation. We indicate only the general trend.

For $H \gtrsim 11.5$ cm, the onset of unsteady behaviour leads to side kicks rather than meandering. For $H \approx 11.5$ cm, this onset is sufficiently repeatable to determine the critical values of U_0 (the data are plotted in figure 6), but for $H \gtrsim 12$ cm, unsteadiness can be triggered by small disturbances over a range of U_0 and it was thus not possible to determine the boundary between steady and unsteady behaviour.

For the larger values of U_0 in the unsteady regime, the oscillations are generally irregular, but can be thought of as an apparently random sequence of side kicks, meanders and figures-of-eight. That is to say, the thread exhibits similar types of motion to these regimes, but continues to switch between them instead of settling down to a particular one. An example is shown in figure 5(*e*), where the pattern is rapidly shifting, but shows characteristics of side kicks, coiling and possibly figures-of-eight. One exception to this irregularity is a window of stability for a regular figure-of-eight pattern near $H \approx 12$ cm (figure 5*d*), which is distinct from the figure-of-eight window for $H < 8$ cm (figure 4*d*, *e*). It is also possible to obtain the 'double-8' pattern in this range.

For the smaller values of U_0, the tail of the thread exhibits rapid coiling. The coiling was often irregular, with successive loops being of different sizes and the sense of rotation changing episodically. Irregularity was particularly associated with speeds such that there was significant overlap between successive coils. The persistence of irregularity to large values of H can be contrasted with the case of coiling on a stationary surface for which irregularity is observed in an intermediate range of heights, but is stabilized again at large heights (Maleki *et al.* 2004).

Variation with experimental parameters

The parameters Q, d and ν were varied between experiments (table 1), though not completely independently owing to the gravity-fed source. We regard Q and ν as the primary parameters, since the theory of § 4 shows that changing the value of d merely corresponds to a small offset in H.

Regime diagrams were obtained for experiments 2–8, and were all qualitatively the same as figure 6 with regard to the relative location and transitions between different patterns. Indeed, there was little quantitative difference between the regime diagrams of experiments with the same fluid (hence similar values of ν), but different values of Q. Comparison of experiments with different fluids showed that corresponding regimes occur at smaller heights for syrups with a smaller viscosity; the heights that give corresponding regimes for the three syrups are very roughly in the ratio 1 : 1.2 : 1.6, while the viscosities are roughly in the ratio 1 : 2 : 3.

We conclude that the regime diagram depends on ν, but not significantly on Q over the range studied.

https://doi.org/10.1017/S0022112006002503 Published online by Cambridge University Press

4. Theory and numerical procedure for steady shapes

We now present a simple theory for the steady shape of a stretching catenary based on the slenderness of the thread and the usual extensional-flow approximation. Teichman & Mahadevan (2003) use similar equations to describe the time-dependent sagging of a viscous filament between two fixed supports in the absence of inertia and surface tension.

We include inertial, capillary and gravitational forces, in addition to the viscous resistance to stretching, but neglect both the viscous resistance to bending and the drag from the surrounding air. The neglect of bending resistance is a very good approximation for most of the steady flows, but precludes the buckling mechanism that gives rise to unsteady flow at low belt speeds. Analysis of these unsteady flows requires solution of the full set of coupled bending and stretching equations (Entov & Yarin 1984).

Consider a slender axisymmetric thread falling in a steady arc onto a belt moving at velocity U_0. Let s be the arclength measured from the point of contact with the belt, r the radial coordinate for the local circular cross-section of the thread, $R(s)$ the radius of the thread and $\psi(s)$ the inclination of the centreline to the horizontal. Let u_s and u_r be the components of velocity in the directions s and r. The governing physical parameters are the source diameter d, flow rate Q, surface tension γ, density ρ, viscosity μ or kinematic viscosity ν, and gravity g.

The slenderness of the thread and the neglect of shear stresses due to air drag means that the flow can be assumed to be locally uniform, i.e. $u_s \equiv -U(s)$, where the minus sign is introduced so that $U > 0$ for a thread falling from $s > 0$ towards a contact with the belt at $s = 0$. From conservation of mass, we deduce that $u_r = (r/2)\,\mathrm{d}U/\mathrm{d}s$.

The radial stress balance at the free surface $r = R$ then gives the fluid pressure as

$$p = 2\mu\frac{\partial u_r}{\partial r} + \frac{\gamma}{R} = \mu\frac{\mathrm{d}U}{\mathrm{d}s} + \frac{\gamma}{R}, \tag{4.1}$$

and thus the axial stress is

$$\sigma_{ss} = -p - 2\mu\frac{\mathrm{d}U}{\mathrm{d}s} = -3\mu\frac{\mathrm{d}U}{\mathrm{d}s} - \frac{\gamma}{R}. \tag{4.2}$$

The axial and transverse equations of motion, obtained for example by applying Newton's laws to an infinitesimal slice of fluid of mass $\rho(\pi R^2\,\mathrm{d}s)$, are

$$\pi R^2\rho U\frac{\mathrm{d}U}{\mathrm{d}s} = \frac{\mathrm{d}F_s}{\mathrm{d}s} - \pi R^2\rho g\sin\psi \tag{4.3a}$$

$$\pi R^2\rho U^2\frac{\mathrm{d}\psi}{\mathrm{d}s} = F_s\frac{\mathrm{d}\psi}{\mathrm{d}s} - \pi R^2\rho g\cos\psi, \tag{4.3b}$$

where

$$F_s = \pi R^2\sigma_{ss} + 2\pi R\gamma \tag{4.4}$$

is the total force acting over a cross-section.

Using the steady-state conservation of volume flux,

$$Q = \pi R^2 U, \tag{4.5}$$

we can eliminate R in terms of U. Then, substituting (4.2), (4.4) and (4.5) into the governing equations (4.3a, b), we obtain

$$\frac{\mathrm{d}T}{\mathrm{d}s} = \frac{g\sin\psi}{U}, \quad T\frac{\mathrm{d}\psi}{\mathrm{d}s} = \frac{g\cos\psi}{U}, \tag{4.6}$$

https://doi.org/10.1017/S0022112006002503 Published online by Cambridge University Press

where T is given by

$$UT = -3\nu\frac{\mathrm{d}U}{\mathrm{d}s} - U^2 + \frac{\gamma}{\rho}\left(\frac{\pi U}{Q}\right)^{1/2}. \tag{4.7}$$

The two equations in (4.6) are just the equations for the static equilibrium of a catenary with tension T and weight per unit length U^{-1} (the cross-sectional area is proportional to U^{-1} in a steady state). Hence, T will be referred to as the 'tension', though it has the dimensions of velocity and is the sum of viscous, inertial and capillary forces, with momentum flux regarded as a force.

We make the equations dimensionless using the belt speed U_0 and a length scale characteristic of viscous stretching under gravity. We thus introduce dimensionless variables

$$u(\xi) = \frac{U(s)}{U_0}, \quad \xi = s\left(\frac{g}{3\nu U_0}\right)^{1/2}, \quad t = T\left(\frac{U_0}{3\nu g}\right)^{1/2}, \tag{4.8}$$

so that (4.6) and (4.7) become

$$ut' = \sin\psi, \quad ut\psi' = \cos\psi, \quad ut = -u' - Re\,u^2 + \Gamma\sqrt{u}, \tag{4.9}$$

where primes denote $\mathrm{d}/\mathrm{d}\xi$, and the Reynolds number Re and inverse capillary number Γ are given by

$$Re = \left(\frac{U_0^3}{3\nu g}\right)^{1/2}, \quad \Gamma = \frac{\gamma}{\rho}\left(\frac{\pi}{3\nu g Q}\right)^{1/2}. \tag{4.10}$$

The experimental range of Re was 10^{-3}–10^{-1}, with $O(10^{-2})$ typical, and the range of Γ was 0.4–0.7.

By dividing (4.9*a*) by (4.9*b*), we obtain the first integral

$$t(\xi) = t_0 \sec\psi(\xi), \tag{4.11}$$

where $t_0 = t(0)$ is the dimensionless tension at the contact with the belt. We can then write (4.9) as the coupled differential system

$$u\psi' = \frac{\cos^2\psi}{t_0}, \quad -\frac{u'}{u} - Re\,u + \frac{\Gamma}{\sqrt{u}} = t_0\sec\psi, \tag{4.12}$$

for $\psi(\xi)$ and $u(\xi)$. The dimensionless horizontal displacement x and vertical displacement z are given by solving

$$x' = \cos\psi, \quad z' = \sin\psi. \tag{4.13}$$

Equations (4.12) and (4.13) constitute a fourth-order differential system, which we integrate using a standard Runge–Kutta scheme with adaptive step-size. The boundary conditions at the belt are

$$\psi(0) = 0, \quad u(0) = 1, \quad x(0) = 0, \quad z(0) = 0. \tag{4.14}$$

The dimensionless contact tension t_0 is a free parameter in (4.12) whose value is determined by shooting for the final boundary condition,

$$z = h \equiv H\left(\frac{g}{3\nu U_0}\right)^{1/2} \quad \text{at} \quad u = u_h \equiv \frac{4Q}{\pi d^2 U_0}, \tag{4.15}$$

corresponding to the exit conditions at the nozzle, non-dimensionalized with (4.8). The extensional-flow approximation breaks down within the $O(d)$ distance from the nozzle that it takes for the flow profile to adjust from no-slip to free-slip conditions. However,

https://doi.org/10.1017/S0022112006002503 Published online by Cambridge University Press

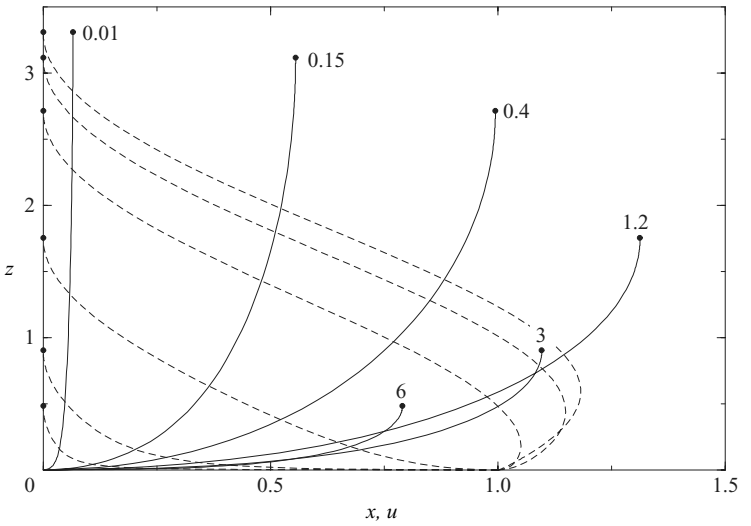


FIGURE 8. Numerical solutions of (4.12)–(4.14) as t_0 is varied for the illustrative values $Re = 0.01$ and $\Gamma = 0.6$, showing the thread shapes $x(z)$ (solid) and velocity profiles $u(z)$ (dotted). The cases shown are $t_0 = 0.01$, 0.15, 0.4, 1.2, 3, 6. The dots at the end of each curve mark the limiting height h^* at which $u \to 0$.

$d \ll H$ and this near-nozzle adjustment makes a negligible difference to the computed solutions. We also note that the average exit velocity $4Q/\pi d^2$ ranged from 0.03 to 0.17 cm s^{-1}, much smaller values than the range of belt speeds $U_0 = 1$–20 cm s^{-1}, and so u_h was typically of order $10^{-2} \ll 1$.

In § 4.1 and § 4.2, we describe the general features of numerical solutions of (4.12)–(4.14) as t_0 is varied without imposing (4.15). In § 5, we re-introduce the boundary condition (4.15) to compare the numerical and experimental results. We consider the thread shapes in § 5.1, and compare the loss of theoretical solution as $t_0 \to 0$ to the experimentally found stability boundary between steady and unsteady behaviour in § 5.2.

4.1. *Numerical solutions*

In order that solutions to (4.12)–(4.14) lie in the positive quadrant $x > 0, z > 0$, corresponding to a thread falling with $u > 0$ towards contact with the belt at the origin, it is necessary that $t_0 > 0$; from (4.12*a*), the equations become singular as $t_0 \to 0$, and for $t_0 < 0$ solutions in $x > 0$ lie in $z < 0$, which is unphysical. We note also from (4.12*a*) that $\psi' > 0$ and hence it is not possible for this extensional-flow theory to reproduce the backward tilting heel shapes (e.g. figure 2*d*) that are typically observed over a small range of belts speeds intermediate between those that give an apparently vertical thread and those which mark the onset of unsteadiness.

Figure 8 displays the thread shapes $x(z)$ and velocities $u(z)$ for a range of values of t_0 with $t_0 > 0$. The illustrative parameter values $Re = 0.01$ and $\Gamma = 0.6$ are typical of the experiments, and the qualitative form of the figure would be the same for other values. We see from figure 8 that small values of t_0 give an almost vertical thread, whereas large values of t_0 give a thread that is largely being dragged sideways. For large values of t_0, the fluid accelerates monotonically from the source to the contact with the belt at the origin, whereas for small values of t_0 the thread undergoes a small region of deceleration as it approaches the belt.

https://doi.org/10.1017/S0022112006002503 Published online by Cambridge University Press

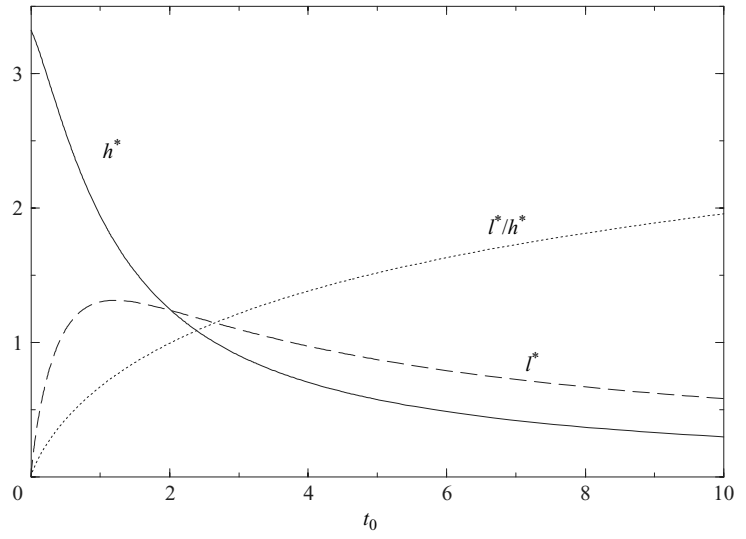


FIGURE 9. The limiting height h^* and horizontal displacement l^* at which $u=0$ as t_0 is varied for $Re=0.01$ and $\Gamma=0.6$. The ratio l^*/h^* is also shown.

An important feature of figure 8 is that all solutions terminate at some finite limit point where $u\to 0$ (hence $R\to\infty$) and $\psi\to\pi/2$ (a vertical thread). It can be shown (see Appendix B) that the asymptotic behaviour near this limit is given by

$$u\left[(8+\Gamma^2)^{1/2}+\Gamma\right]^2 \sim 4(\xi^*-\xi)^2, \tag{4.16}$$

where ξ^* is the dimensionless arclength at the limit point. We denote the corresponding limiting height and horizontal displacement by $h^*=z(\xi^*)$ and $l^*=x(\xi^*)$, respectively.

Figure 9 shows the variation of the limiting values $h^*(t_0)$, $l^*(t_0)$ and $l^*(t_0)/h^*(t_0)$ with t_0. We observe first that the limiting height h^* is a monotonically decreasing function of t_0. The actual dimensionless fall height h is given by the boundary condition (4.15). Since $Q\ll\pi d^2U_0/4$, we note that $u_h\ll 1$ and hence $h\approx h^*$. This suggests that h is also a monotonically decreasing function of t_0, and this has been verified numerically. Hence there is a unique solution for t_0 given the boundary condition (4.15). It also follows from (4.15) that increasing t_0 and thus decreasing h corresponds, if the dimensional fall height H is fixed, to increasing the belt speed U_0. (The explicit dependence of (4.15) on U_0 is much stronger than any implicit dependence through the variation of h with Re.) We observe secondly from figure 9 that, though the limiting horizontal displacement l^* has a maximum at $t_0\approx 1.2$, the ratio l^*/h^* is a monotonically increasing function of t_0. Thus, when the results are redimensionalized to a fixed fall height H, the dimensional horizontal displacement L is a monotonically increasing function of t_0 and hence of U_0, as expected.

4.2. *Loss of solution as* $t_0\to 0$

We have already noted the constraint $t_0>0$. From figures 8 and 9, we can now also say that the limit $t_0\to 0$ gives a (nearly) vertical thread and the maximum value of h^*, which we denote by $h^*_m(\Gamma, Re)$. The limit $t_0\to 0$ also gives the maximum value of the dimensionless fall height h. From (4.15), we deduce that, in dimensional terms for fixed H, this corresponds to a minimum value of U_0: there is no solution to the steady extensional-flow model for smaller values of U_0. In § 5.2, we compare this

https://doi.org/10.1017/S0022112006002503 Published online by Cambridge University Press

Experiment	Γ	$h_v^*(\Gamma, 0)$	H_0 (cm)	α $(\mathrm{cm\,s})^{-1/2}$	A
2	0.655	3.48	0.463	0.266	0.220
3	0.579	3.29	0.415	0.275	0.242
4	0.594	3.33	0.407	0.297	0.255
5	0.453	3.01	0.406	0.322	0.279
6	0.614	3.38	0.491	0.364	0.326
7	0.694	3.58	0.450	0.472	0.377
8	0.646	3.45	0.386	0.497	0.397

TABLE 2. The main parameters in the theoretical prediction $U_0^{1/2} = \alpha(H + H_0)$ for loss of an extensional solution, see (4.19), and the experimental best fit of the form $U_0^{1/2} = A(H + H_0)$ for the onset of unsteadiness.

loss of solution as $t_0 \to 0$ to the experimental boundary between steady and unsteady behaviour.

As $t_0 \to 0$, equation (4.12a) becomes singular and thus the change in ψ from the boundary value $\psi(0) = 0$ to the interior value $\psi \sim \pi/2$ occurs in a thin boundary layer of width $O(t_0)$. In the boundary layer, u' and t' are $O(1)$, and so t remains $O(t_0)$ and $u \sim u(0) = 1$. Equation (4.12a) is thus solved to give $\psi \sim \tan^{-1}(\xi/t_0)$. The thread is therefore vertical outside the boundary layer and the vertical displacement z has (almost) the same value as the arclength ξ. The solution outside the boundary layer is most easily derived by returning to (4.9) with $\psi = \pi/2$ to obtain

$$ut' = 1 \quad \text{where } t = -\frac{u'}{u} - Re\, u + \frac{\Gamma}{\sqrt{u}}. \tag{4.17}$$

Matching to the boundary layer gives boundary conditions $u(0) \sim 1$ and $t(0) \sim 0$.

As in the full equations (4.9), all solutions of (4.17) (with $u > 0$ and $t \geqslant 0$) terminate at some finite height where $u \to 0$ in the manner described by (4.16) (see Appendix B). The limiting height for the boundary conditions $u(0) = 1$ and $t(0) = 0$ is, of course, equal to the value $h_m^*(\Gamma, Re)$ obtained from h^* as $t_0 \to 0$.

Since $u_h \ll 1$, we can derive a very good approximation for the belt speed at which there is a loss of solution by substituting the boundary condition $u = u_h$ at $\xi = h$ into (4.16) to obtain

$$h_m^* = h + \frac{u_h^{1/2}}{2}\left[(8 + \Gamma^2)^{1/2} + \Gamma\right]. \tag{4.18}$$

On redimensionalizing this result with (4.15), we obtain

$$U_0^{1/2} = \alpha(H + H_0) \quad \text{where } \alpha = \left(\frac{g}{3\nu h_m^{*2}}\right)^{1/2}, \quad H_0 = \left(\frac{3\nu Q}{\pi d^2 g}\left[(8 + \Gamma^2)^{1/2} + \Gamma\right]\right)^{1/2}. \tag{4.19}$$

The coefficient α depends on U_0 through the dependence of h_m^* on Re, but only very weakly when $Re \ll 1$. The values of these parameters for $Re = 0$ are shown in table 2.

5. Comparison of theory and experiment

Images of the catenary shapes formed by the thread in the steady regime were obtained by processing stills from a digital movie of the experiments (cf. figure 2).

https://doi.org/10.1017/S0022112006002503 Published online by Cambridge University Press

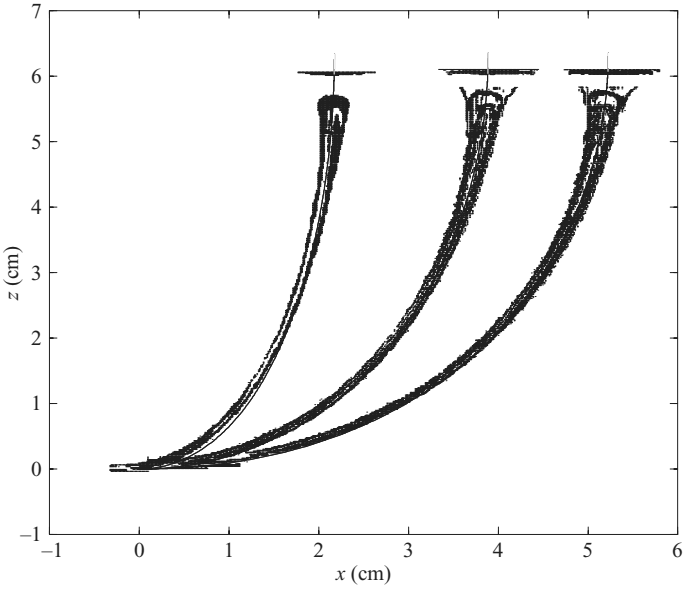


FIGURE 10. Calculated thread shapes (solid curves) and pixelated images of experiment 1. Here $H = 6.05$ cm and $U_0 = 4.66$, 8.3 and 14.5 cm s^{-1}, respectively from left to right.

Since the small ($< 5\,\%$) variations in belt speed during one revolution of the belt caused slight oscillations of the shape, we chose the movie frame nearest the middle of the oscillation, this corresponding most closely to the measured average belt speed. Image-processing software was then used to separate the yellow Golden Syrup from the darker background and thence to produce a pixelated image of the thread. Lighting effects prevented the edges of the thread being measured with sufficient precision to enable comparison of the thread thickness with theory. However, the edges in the pixelated image do give a reliable indication of the centreline of the thread for comparison with the theoretical shapes. The scale of the image was determined from a ruler in the field of view, and the origin of the image was fixed by the midpoint of the bottom of the nozzle. This scale and origin were used to resize and align the image against the theoretical predictions of the thread centreline. These predictions were obtained with the numerical method described in § 4.

5.1. *Shape of catenary*

We compared the numerically predicted and experimentally observed shapes over a range of heights, belt speeds and tube diameters. Figure 10 is a typical comparison, which displays shapes from experiment 1 at a fixed fall height $H = 6$ cm for three different belt speeds U_0. The three theoretical curves contact the belt at the origin, and the three pixelated images have been scaled and shifted to match the top of the thread in the manner described above. The curves obtained numerically show good agreement with experiment, and similar agreement was found in all cases where the belt speed is sufficiently large to pull the thread away from vertical; as noted earlier, the theoretical model is unable to match the heel shapes produced at low speeds when the thread is near vertical.

In figure 11, we compare the theoretical prediction with the measured horizontal displacement of the thread as U_0 was varied at a fixed fall height $H = 7$ cm in experiment 9. The contact point between the belt and the thread was most easily

https://doi.org/10.1017/S0022112006002503 Published online by Cambridge University Press

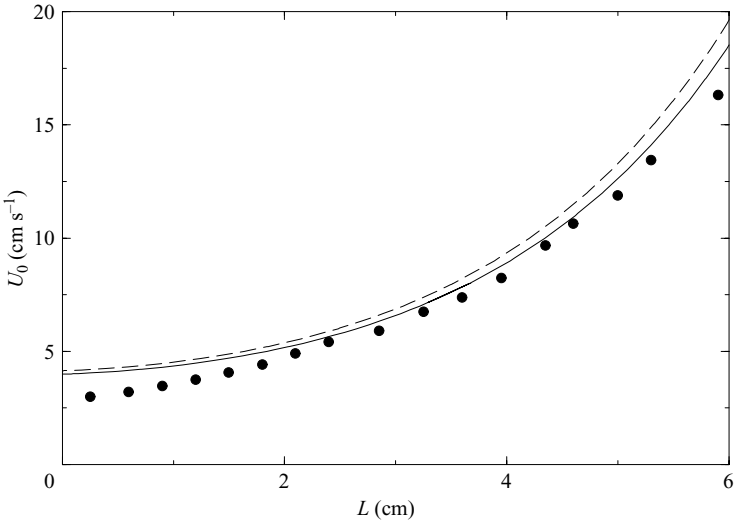


FIGURE 11. Horizontal displacement L for $H = 7$ cm in experiment 9 (dots), with the theoretical predictions for viscosities corresponding to 21.25 °C (solid) and 21.75 °C (dashed). The discrepancy at low belt speeds cannot be explained by uncertainty in the viscosity and is largely accounted for by the neglected bending stresses.

identified by eye, and the horizontal displacement was measured using a ruler mounted just above the belt for this purpose. The theoretical predictions depend on the fluid viscosity, and the dashed and solid lines correspond to the viscosity at the temperatures measured at the beginning and end of the experiment, respectively.

The agreement between theory and experiment is quite good, particularly at the larger belt speeds and if the larger viscosity (lower temperature) is assumed. We note, however, that the theory curves consistently predict smaller horizontal displacements than observed and that the discrepancy is particularly marked for displacements less than about 2 cm (belt speeds less than about 5 cm s^{-1}). As discussed in § 6, we do not believe that this discrepancy should be explained simply as an under-estimate of the viscosity.

5.2. *Loss of steady solution and onset of unsteadiness*

Figure 6 showed that the boundary between steady and unsteady behaviour in experiment 3 was approximately of the form $U_0^{1/2} \propto H$. Figure 12 shows more detailed experimental data for this boundary from experiments 5 and 7, including error bars marking repeatable observations of clear steady and oscillatory behaviour on either side of the transition. These plots are typical of the results from all the experiments (2–8) in which such measurements were made. In all cases, the steady–unsteady boundary is approximately linear in H and $U_0^{1/2}$, particularly if the lowest point or two is omitted.

A partial understanding of this result can be obtained by comparison with (4.19). Since Re was typically of order 10^{-2}, we can replace $h_m^*(\Gamma, Re)$ by $h_m^*(\Gamma, 0)$ to a very good approximation. Moreover, Γ depends only on parameters held constant in each experiment and not on the belt speed U_0. Therefore, for a given experiment, H_0 is constant and α is approximately constant, and thus (4.19) gives another linear relationship between H and $U_0^{1/2}$, in this case for the loss of a steady extensional

https://doi.org/10.1017/S0022112006002503 Published online by Cambridge University Press

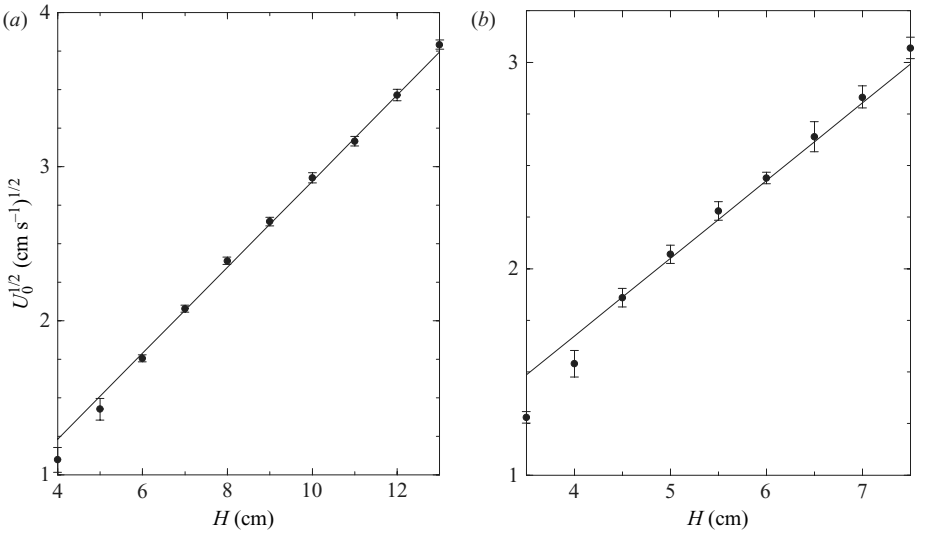


FIGURE 12. The belt speed U_0 (cm s^{-1}) at the steady–unsteady boundary as a function of height H for (*a*) experiment 5 and (*b*) experiment 7. The linear fits are constrained to have the intercept given by that of (4.19).

solution. The values of the gradient α (table 2) can be found by a single numerical integration of (4.17) with $Re = 0$ for each experiment.

To compare the loss of theoretical solution with the experimental boundary between steady and unsteady behaviour, we fitted the experimental data with straight lines of the form $U_0^{1/2} = A(H + H_0)$, where the offset H_0 from (4.19) is imposed and the gradient A is chosen to give the best fit. Figure 12 shows these straight-line fits for experiments 5 and 7. (The value of H_0 in each experiment is typically only a few millimetres (see table 2). Nevertheless, it is a very good approximation to $H^* - H$ for all steady solutions and it seems sensible to impose this offset, even though it does not make much difference to the fit.)

Figure 13 compares the fitted experimental gradients A with the theoretical gradients α of (4.19). Viscosity causes the main variation in α, with the tube diameter d having a smaller effect through its effect on Q and hence Γ. The figure shows a strong linear correlation between the two gradients, but the experimental gradients are consistently only about 85 % of the theoretical gradients. This discrepancy is not due to the neglect of inertia: while the relationship (4.19) is slightly nonlinear for $Re > 0$, the effect on the average gradient is only about 2 % in the parameter regime of interest. We believe the discrepancy is primarily due to bending stresses starting to play a significant role when the belt speed becomes sufficiently small for the lowest part of the thread to be in compression. In support of this view, we note that the thread is observed to have a backward tilting heel over most of the range of belt speeds between the loss of an extensional solution and the onset of unsteadiness.

6. Discussion

In this paper, we have presented a first experimental investigation of the behaviour of a viscous fluid thread falling onto a steadily translating horizontal surface or belt. A surprising variety of behaviours has been uncovered, ranging from steady stretching flow at high belt speeds, through a complex set of oscillatory regimes at intermediate

https://doi.org/10.1017/S0022112006002503 Published online by Cambridge University Press

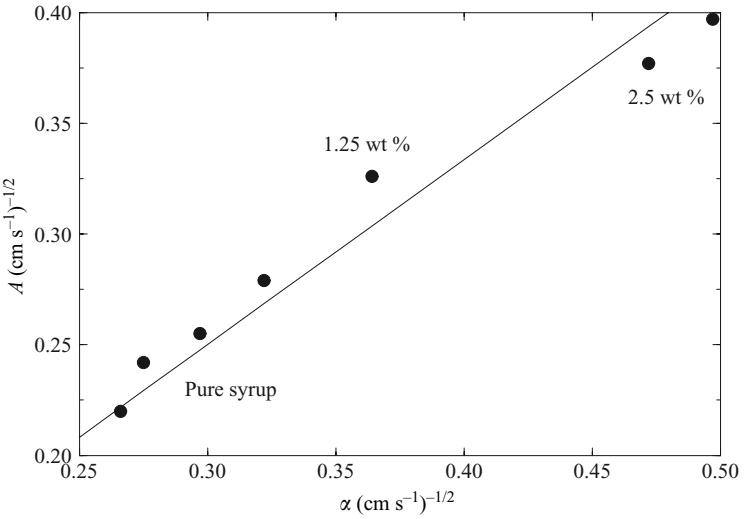


FIGURE 13. Comparison of the gradients A and α in the best fits of the form $U_0^{1/2} = A(H + H_0)$ for the onset of unsteadiness in experiments 2–8 and the corresponding theoretical predictions $U_0^{1/2} = \alpha(H + H_0)$ for loss of an extensional solution (see (4.19)). The numerical values of A and α are given in table 2. The fitted line is $A = 0.834\alpha$.

speeds, to steady coiling at low or zero speeds. The main limitations on the quantitative accuracy of the results are probably due to the small (<5 %) variations in belt speed during a revolution of the belt and to the sensitivity of the viscosity of Golden Syrup to small variations of temperature. The variation of belt speed, in particular, prevented a definitive delineation of all the stability boundaries between the different modes of oscillation, but we do not believe that it affected either the qualitative observations of the different modes or the structure of the regime diagram. Future, better engineered experiments could quantify the frequency and shape of the oscillations, as well as the stability boundaries of the more unusual modes of oscillation.

We have also presented a simple theory based on extensional flow of a slender thread for the steady shapes produced by high belt speeds. This gives good agreement with both the experimentally observed shapes and the horizontal displacements when the belt speed is sufficiently large to pull the thread away from vertical. In this situation, the thread is in tension throughout its length, bending stresses are only a small perturbation and the shape is that of a catenary of non-uniform mass per unit length. An important feature of the theory is the loss of solution if the belt speed is reduced below a critical value, corresponding to the lowest part of the thread entering into compression. Near this critical value, the thread is nearly vertical, bending stresses are very significant where the thread turns through 90° close to the belt, and a 'heel' shape is observed experimentally. We also note that bending stresses are generally more important at small fall heights and large flow rates because the thread is then thicker. In calculations to be reported elsewhere, we show that a more complicated theory incorporating the bending stresses is capable of predicting the heel shape and giving good agreement with the horizontal displacement, even for near vertical threads. We also found that the experimental onset of unsteadiness is closely correlated to the loss of the extensional-flow solution, though it consistently occurs at a lower speed. This is presumably due to the need for a certain length of the thread

https://doi.org/10.1017/S0022112006002503 Published online by Cambridge University Press

to be in compression if the bending stiffness is to be overcome and buckling to ensue. The loss of solution thus provides an upper bound for the onset of unsteadiness.

The main observation lacking a theoretical explanation is the variety of oscillatory patterns. Some qualitative understanding is provided by noting that many of the patterns on the belt are produced by sideways, circular and figure-of-eight oscillations of the thread, which can be thought of as Lissajous figures with frequency ratios (lateral motion:longitudinal motion) of 1:0, 1:1 and 1:2. Among the 1:2 modes, it should be noted that the figure-of-eight pattern has the opposite phase relationship to meandering and braiding, that the W pattern has a markedly broken symmetry, and that the slanted-loop pattern is rotated relative to the belt motion. The occurrence of some of these patterns in fairly wide regions of parameter space suggests that the frequency-2 component of motion may be a simple consequence of nonlinearity, though the phase relationships and the symmetry breaking still lack an explanation. The W, double-8 and double-meander patterns occur over a narrow range of heights, which suggests that these modes may be related to some sort of resonance between different inertial oscillations of the thread. Indeed, we note that the range of heights over which there is well-defined hysteretic behaviour (8–11 cm in figure 6) is very similar to the inertio-gravity regime identified by Ribe *et al.* (2006) in which there are multiple solutions for the coiling frequency on a stationary surface. Finally, we note again the evidence provided by the tilting of 'slanted loops' and the fusion in 'double-coiling' for the importance of perturbations to the thread caused by intersection with the laid-down pattern. It is not clear how the moving contact-point conditions of Skorobogatiy & Mahadevan (2000) and Ribe (2004) should be generalized to include such effects.

It has taken over forty years to disentangle the different dynamical regimes of the relatively simple phenomenon of 'fluid rope-coiling'. We hope that recent advances in experimental, numerical and theoretical techniques will allow for a speedier understanding of the stitching patterns of the 'fluid-mechanical sewing machine'.

We are very grateful to Keith Moffatt and Jae-Tack Jeong for the inspiration provided by their preliminary investigations of this problem, and to Neil Ribe for many interesting discussions. S.C. was supported by a summer research studentship from Trinity College, Cambridge. J.R.L. acknowledges generous hospitality from the Institut de Physique du Globe, Paris during the writing of this paper.

Appendix A. Fluid parameters

The viscosity of Golden Syrup varies quite strongly with temperature, with a 1 °C change in temperature producing about a 20 % change in viscosity. The room temperature θ was recorded both before and after each experiment to the nearest 0.25 °C, and the syrup temperature was taken to be the same as the room temperature. The inverse exponential relationship found in both Davaille & Jaupart (1993) and White (1988) was then used to calculate the viscosity ν from the temperature θ in °C:

$$\nu = \nu_0 \exp\left(\frac{1}{A\theta^2 + B\theta + C}\right), \tag{A 1}$$

with

$$\nu_0 = 3.33 \times 10^{-7}\,\mathrm{cm^2\,s^{-1}}, \tag{A 2}$$

$$A = -7.5907 \times 10^{-7}, \quad B = 3.8968 \times 10^{-4}, \quad C = 4.0130 \times 10^{-2}. \tag{A 3}$$

https://doi.org/10.1017/S0022112006002503 Published online by Cambridge University Press

The values of the coefficients A, B and C were taken directly from Davaille & Jaupart (1993), while ν_0 was inferred from a viscosity measurement at known temperature with a falling ball viscometer. (Use of the values of A, B and C from White (1988) instead of those from Davaille & Jaupart (1993) with the corresponding inferred value of ν_0 gave a negligible difference over the narrow working range 20.5–22.5 °C.) The values of A, B and C in (A 3) were also used to calculate the viscosity of diluted syrup, with $\nu_0 = 2.33 \times 10^{-7}\,\mathrm{cm^2\,s^{-1}}$ for 1.25 wt% added water and $\nu_0 = 1.08 \times 10^{-7}\,\mathrm{cm^2\,s^{-1}}$ for 2.50 wt% added water as inferred from a viscosity measurement obtained with a U-tube viscometer. (It was checked that the use of the values of A, B and C reported for 10 wt% water in Davaille & Jaupart (1993) again gave a negligible difference over the narrow working temperature range.)

The density of the Golden Syrup was measured to be $1.438 \pm 0.002\,\mathrm{g\,cm^{-3}}$, in agreement with the value reported by Davaille & Jaupart (1993), and the density of syrup diluted with water was calculated by assuming linear mixing.

The *CRC Handbook of Chemistry and Physics* (Weast 1984) lists surface tensions for sucrose solutions of concentration 0–55 wt%. An approximate extrapolation to the 82.5–83.0 % sucrose concentration of Golden Syrup (C. Knolls, Tate & Lyle plc, personal communication) gives a surface tension of about $78\,\mathrm{dyn\,cm^{-1}}$, in good agreement with the value of $80\,\mathrm{dyn\,cm^{-1}}$ (± 10 %) reported by Llewellin, Mader & Wilson (2002). A surface tension value of $78\,\mathrm{dyn\,cm^{-1}}$ was also used for syrup with 1.25 and 2.50 wt% added water, since the change in sucrose concentration is too small to make a significant difference. Neither surface tension nor density is expected to vary significantly over the temperature range of the experiments.

Appendix B. Asymptotic solution near the nozzle

Consider solutions of (4.12) with $u > 0$, $t_0 > 0$ and $0 \leqslant \psi < \pi/2$ corresponding to a thread falling in the positive quadrant towards the origin. We note from (4.12*b*) that $u(\xi)$ is bounded above since $u' < 0$ if $u > (\Gamma/t_0)^2$. From (4.12*a*) we see that $\psi(\xi)$ increases monotonically and, since u is bounded, $\psi \to \pi/2$. We set $\overline{\psi} = \pi/2 - \psi$ and rewrite (4.11) and (4.12) as

$$t = \frac{t_0}{\sin\overline{\psi}} = -\frac{u'}{u} - Re\,u + \frac{\Gamma}{u^{1/2}}, \qquad ut' = \cos\overline{\psi}. \tag{B 1}$$

We deduce from (B 1*a*) that $t \to \infty$ and $u \to 0$ as $\overline{\psi} \to 0$. In this limit,

$$\frac{u'}{u} - \frac{\Gamma}{u^{1/2}} + t = O(Re\,u), \qquad ut' = 1 + O((t_0/t)^2). \tag{B 2}$$

A leading-order balance of terms in (B 2) gives $u \sim (\xi^* - \xi)^2$, $t \sim (\xi^* - \xi)^{-1}$ and $\overline{\psi} \sim t_0(\xi^* - \xi)$ as $\xi \to \xi^*$, where ξ^* is the finite arclength at which the limit $\overline{\psi} \to 0$ is attained. More detailed analysis shows that

$$u = 4(\xi^* - \xi)^2/C^2 + O\left(t_0^2(\xi^* - \xi)^4, Re(\xi^* - \xi)^5, (\xi^* - \xi)^{4+\Gamma C/4}\right), \tag{B 3}$$

where $C = \Gamma + (\Gamma^2 + 8)^{1/2}$. The first two correction terms in (B 3) are forced directly by the correction terms in (B 2); the third correction term (with exponent dependent on Γ) is an eigenmode of the linearization of (B 2) about the leading-order solution, and occurs with a magnitude determined by the boundary conditions. Similar expansions are readily derived for t and $\overline{\psi}$.

For the case of a vertical thread, we can perform a similar analysis of (4.17). If $u(0) > 0$ and $t(0) \geqslant 0$, then u is bounded above, t increases monotonically to ∞ and

https://doi.org/10.1017/S0022112006002503 Published online by Cambridge University Press

$u \to 0$. The limiting behaviour is given by (B 2) with $t_0 = 0$. Thus (B 3) also applies, but without the first correction term, as could also have been derived by considering the limit $t_0 \to 0$. Since $(h^* - h)^2$ and Re were both typically of order 10^{-2}, we note in particular that (B 3) is an excellent approximation for $\xi = h$ in the limit $t_0 \to 0$, i.e. for $\xi = h_m$, confirming the validity of (4.18).

REFERENCES

Barnes, G. & MacKenzie, J. 1959 Height of fall versus frequency in liquid rope-coil effect. *Am. J. Phys.* **27**, 112–115.

Barnes, G. & Woodcock, R. 1958 Liquid rope-coil effect. *Am. J. Phys.* **26**, 205–209.

Cruickshank, J. O. & Munson, B. R. 1983 A theoretical prediction of the fluid buckling frequency. *Phys. Fluids* **26**, 928–930.

Davaille, A. & Jaupart, C. 1993 Transient high-Rayleigh-number convection with large viscosity variations. *J. Fluid Mech.* **253**, 141–161.

Entov, V. M. & Yarin, A. L. 1984 The dynamics of thin liquid jets in air. *J. Fluid Mech.* **140**, 91–111.

Griffiths, R. W. & Turner, J. S. 1988 Falling of viscous plumes impinging on a density of viscosity interface. *Geophys. J.* **95**, 397–419.

Llewellin, E. W., Mader, H. M. & Wilson, S. D. R. 2002 The rheology of a bubbly liquid. *Proc. R. Soc. Lond.* A **458**, 987–1016.

Mahadevan, L. & Keller, J. B. 1996 Coiling of flexible ropes. *Proc. R. Soc. Lond.* A **452**, 1679–1694.

Mahadevan, L., Ryu, W. S. & Samuel, A. D. T. 1998 Fluid 'rope trick' investigated. *Nature* **392**, 140.

Mahadevan, L., Ryu, W. S. & Samuel, A. D. T. 2000 Correction: fluid 'rope trick' investigated. *Nature* **403**, 502.

Maleki, M., Habibi, M., Golestanian, R., Ribe, N. M. & Bonn, D. 2004 Liquid rope coiling on a solid surface. *Phys. Rev. Lett.* **93**, 214502.

Skorobogatiy, M. & Mahadevan, L. 2000 Folding of viscous sheets and filaments. *Europhys. Lett.* **52**, 532–538.

Ribe, N. M. 2003 Periodic folding of viscous sheets. *Phys. Rev.* E **68**, 036305.

Ribe, N. M. 2004 Coiling of viscous jets. *Proc. R. Soc. Lond.* A **460**, 3223–3239.

Ribe, N. M., Huppert, H. E., Hallworth, M. A., Habibi, M. & Bonn, D. 2006 Multiple coexisting states of liquid rope coiling. *J. Fluid Mech.* **555**, 275–297.

Taylor, G. I. 1969 Instability of jets, threads, and sheets of viscous fluid. *Proc. 12th Intl Congr. Appl. Mech.*, pp. 382–389, Springer.

Teichman, J. & Mahadevan, L. 2003 The viscous catenary. *J. Fluid Mech.* **478**, 71–80.

Weast, R. C. (ed.) 1984 *CRC Handbook of Chemistry and Physics*, 64th ed, p. F-31. CRC Press.

White, D. B. 1988 The planforms and onset of convection with a temperature-dependent viscosity. *J. Fluid Mech.* **191**, 247–286.

https://doi.org/10.1017/S0022112006002503 Published online by Cambridge University Press